Supplementary Information (SI) for Nanoscale.
This journal is © The Royal Society of Chemistry 2026

Supplementary Information for:

"From resilience to scratch resistance: Engineering the deformation mechanisms of nanostructured surfaces"

Mehmet Kepenekci, Kun-Chieh Chien, Natalia A. Rueda Guerrero, Kwon Sang Lee, and Chih-Hao Chang*

Walker Department of Mechanical Engineering, The University of Texas at Austin, Austin, TX 78712

*Corresponding email: chichang@utexas.edu

Supplementary Information A: Fabrication of Nanostructures

The silicon nanopillar arrays are patterned in photoresist using Lloyd's mirror interference lithography. Then pattern then transferred to the underlying substrates inductively coupled plasma reactive ion etching (ICP-RIE) processes, as illustrated in the schematic shown in Figure S1 (a). The detail of the fabrication process of high aspect ratio periodic silicon nanostructures is reported previously.[1] For sapphire nanopillar fabrication, a polysilicon mask is used to increase the etch depth. The fabrication process follows similar steps to silicon nanopillars as illustrated in Figure S1 (b) and reported previously.[2]

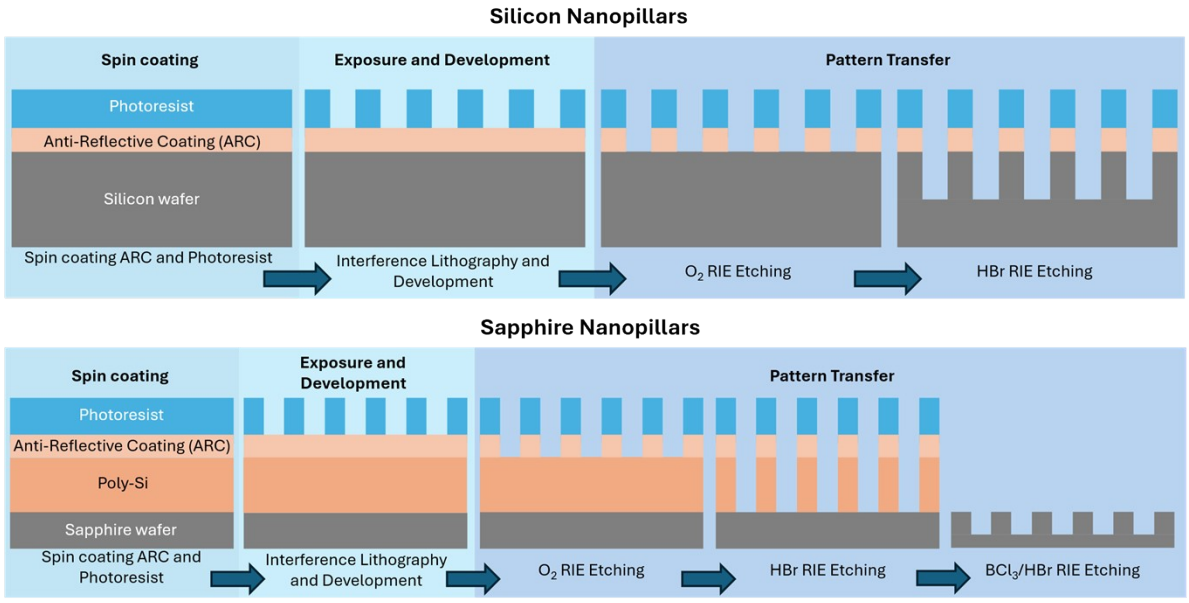

Figure S1. Schematic illustration for (a) silicon, and (b) sapphire nanostructure fabrication process.

Supplementary Information B: Nanoindentation Test

The nanoindentation tests are performed using a conospherical indenter with 10 μm tip radius and 90° cone angle. A representative nanoindentation test with quantities used in calculations is shown in Figure S2.

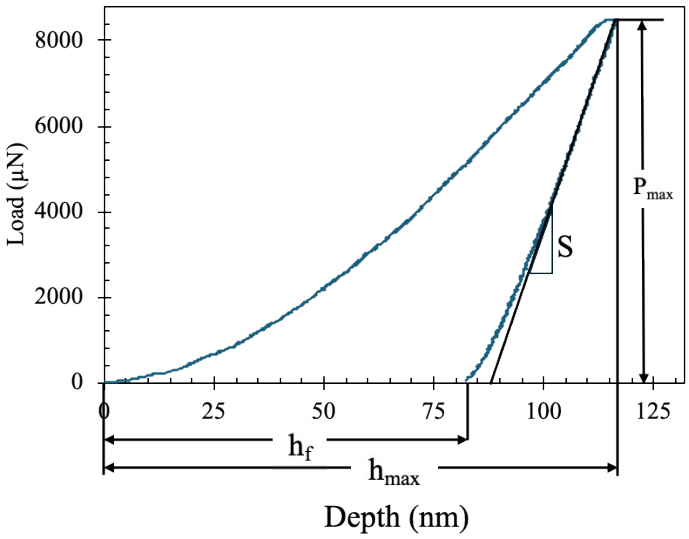

Figure S2. A representative cyclic nanoindentation test on sapphire nanostructures.

The hardness and indentation modulus are calculated using the Oliver-Pharr method. The unloading curve could be approximated by following power law relation.

$$P = \alpha(h - h_f)^m \tag{S1}$$

where α and m are the power law fitting constants, h is the depth and h_f is the final depth. The unloading data between 20% and 95% of the maximum unloading load, P_{max}, is used to fit a curve in the form of (S1). The slope of the unloading curve, S, is calculated via the derivative of the above equation. Then, the sink-in depth h_s is calculated via equation (S2).

$$h_s = \epsilon\frac{P_{max}}{S} \tag{S2}$$

where ϵ is a constant depends on the indenter geometry. Then, the contact depth is calculated using equation (S3).

$$h_c = h_{max} - \epsilon\frac{P_{max}}{S} \tag{S3}$$

The cross-sectional area of the indenter can be approximated using the contact depth to obtain tip area function given in equation (S4).

$$A(h_c) = C_0 h_c^2 + C_1 h_c + C_2 h_c^{1/2} + C_3 h_c^{1/4} + C_4 h_c^{1/8} + C_5 h_c^{1/16} \quad \text{(S4)}$$

The constants, C_n, were obtained empirically based on nanoindentation tests on a fused silica sample. The fitted constants are given in Table S1.

Table S1. Values of fitting constants

Constants	Fitted Constants
C_0	-3.141593
C_1	193006.518
C_2	-11177577.9
C_3	105428227.5
C_4	-254712610.1
C_5	161000362.4

Using the maximum load, P_{max}, and the tip area found using the contact depth and tip area function, hardness, H, is calculated using (S5).

$$H = \frac{P_{max}}{A} \quad \text{(S5)}$$

The indentation modulus, or reduced modulus, E_r, is calculated using equation (S6).

$$E_r = \frac{\sqrt{\pi}\ S}{2\sqrt{A}} \quad \text{(S6)}$$

For quasi-static tests, the samples are tested with different peak loads that produce maximum indentation depth in the region of 10% of the pillar height to avoid the substrate and densification effect at lower depth.

The low and high aspect ratio silicon nanopillars have distinct deformation behavior as illustrated in Figure S3. Low AR structures initially undergo elastic and plastic deformation, then pillar splitting occurs. The complete pillar failure follows upon increasing the load, and further load increase causes densification. On the other hand, high AR structures initially elastically deform, then buckling occurs. Upon increasing the load, the pillar breaks due to bending stress exceeding material strength. Similar to LAR nanostructures, further increase in load after fracture causes densification.

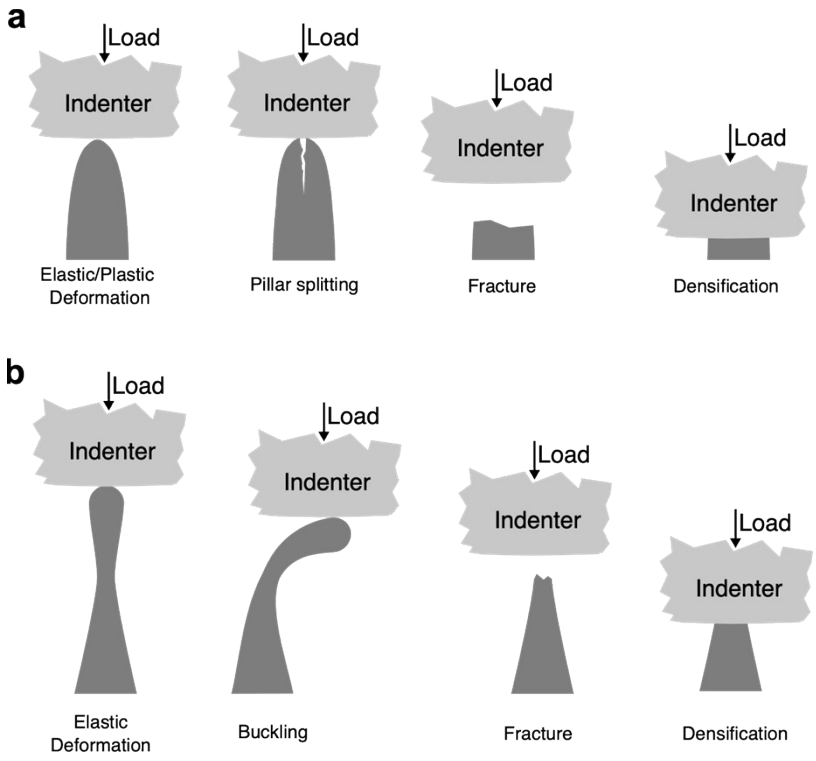

Figure S3. Schematic illustration of (a) LAR and (b) HAR deformation regimes.

The nanoindentation tests are done at multiple points on a rectangular grid. A representative nanoindentation test grid with 25 test points is shown in Figure S4.

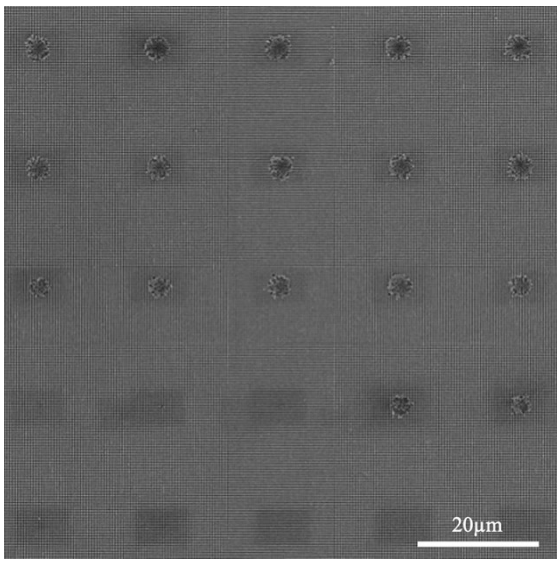

Figure S4. A rectangular array of 25 different nanoindentation tests on LAR silicon sample.

The cyclic tests are done using 10 partial loading and unloading segments, where the probe is unloaded up to 10% of the peak force value of the previous loading segment. This method provides 10 different data points for each test location. The hardness and elastic modulus with standard deviation values are calculated and used in Figure 6(b) and 6(c) and reported with the indentation depth at the corresponding peak load in the loading segment.

The load-depth graphs for the quasi-static nanoindentation tests on sapphire sample is shown in Figure S5.

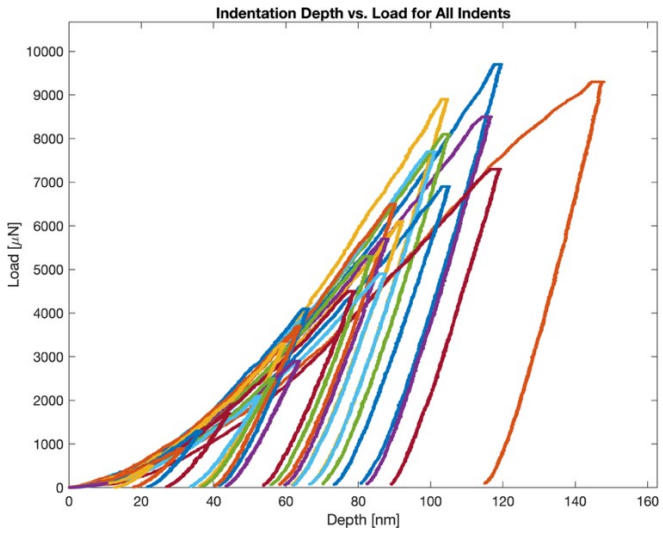

Figure S5. Quasi-static nanoindentation tests on sapphire sample

The load-depth graphs for the quasi-static nanoindentation tests on LAR silicon sample is given in Figure S6 shows the pop-in due to compressive cascade failure around 3000 μN.

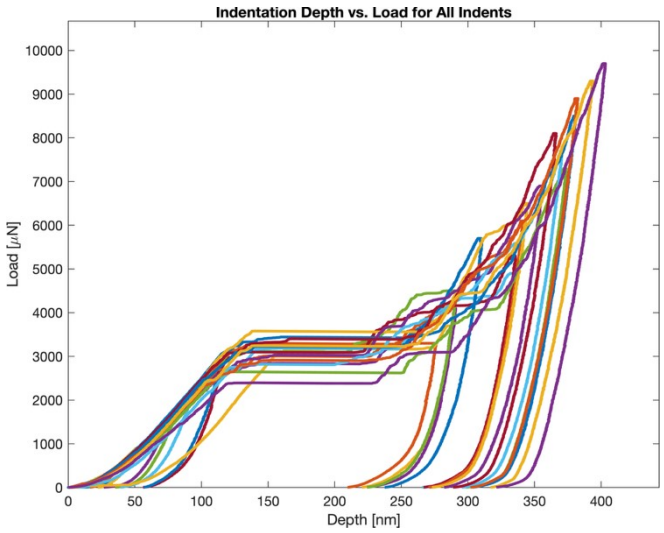

Figure S6. Quasi-static nanoindentation tests on LAR silicon sample

The load-depth curves of the quasistatic tests on HAR silicon with 50 μN maximum load given in Figure S7 shows maximum depth changes from below 50 nm to over 250 nm within the same sample.

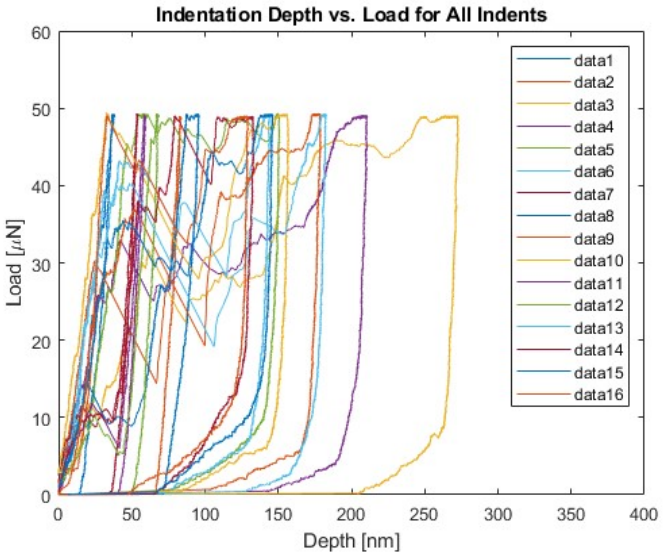

Figure S7. Load vs. depth graph for quasi-static nanoindentations at all 16 different points for high aspect ratio silicon sample.

The variability of the maximum depth is attributed to the variations in the structure geometry. The waist diameter distribution is shown in. Using the SEM images of HAR silicon samples, 60 pillar diameters were measured across 24 different images using ImageJ software. The resulting diameter

distribution is shown in Figure S8. The average diameter and standard deviation are 45.5 nm and 8.6 nm, respectively. The standard deviation corresponds to approximately 20% of the mean diameter, which indicates moderate relative variability in the measured pillar diameters. The reported values correspond to the minimum diameter of each pillar, which coincides with the location at which pillar fracture occurs.

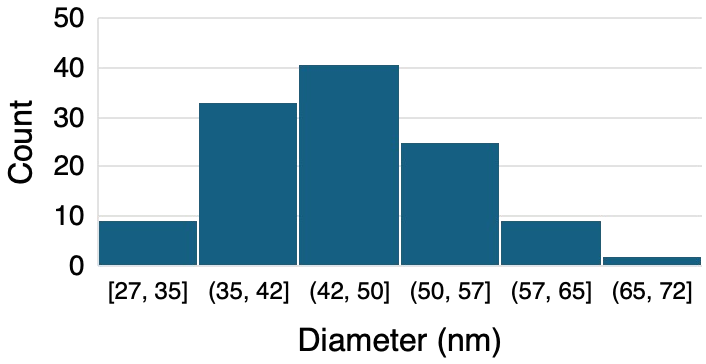

Figure S8. Diameter distribution for HAR silicon nanopillars

Supplementary Information C: Pillar Stress Estimation

To estimate the compressive strength of an individual pillar, the compressive stress each pillar subjected to is calculated by using the geometry of the indenter. The deformation of each pillar is calculated by assuming the indenter is a perfect sphere and does not deform during indentation. Moreover, the load exerted by the indenter is distributed to the pillars according to their deformation. This approach assumes that the force exerted on a pillar is proportional to its deformation. The compressive stress of each pillar is calculated using the calculated force via Eq. S.9, and the area of the pillar obtained from the SEM images of the fractured samples.

$$\sigma_{pillar} = \frac{F_{pillar}}{A_{pillar}} \tag{S.9}$$

Where, σ_{pillar} is the calculated compressive stress, F_{pillar} is the approximated force exerted on the pillar, and A_{pillar} is the cross-sectional area of the pillar. Using this method, the fracture strength of the pillars can be approximated by calculating the compressive stress in the splitting pillar.

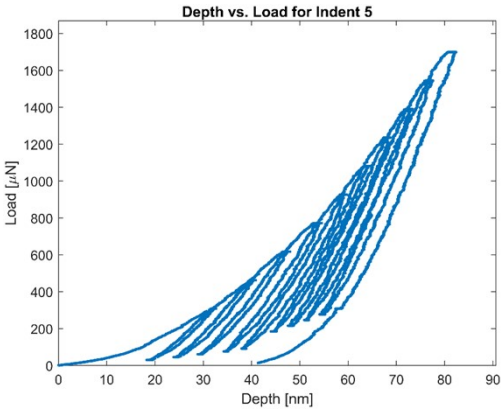

Figure S9. Load vs. depth graph of the split pillar shown in Fig. 4.

The compressive strength of the pillar is calculated using the maximum load in the test, assuming the fracture occurs during the last loading step as fracture is not observed in any of the indents at a lower load at different regions. The same approach is followed to calculate the fracture strength of the sapphire nanopillars. SEM images of the sapphire samples are investigated, and the maximum load of the point at which the first crack is observed is used. The calculated pillar compressive and buckling strength for LAR silicon and sapphire is shown in Table S2.

Table S2. Calculated pillar compressive and buckling strength for the test results presented in Fig. 6.

Material	AR	Compressive/Buckling Strength [GPa]	Failure Mechanism
Sapphire	1.6	10.9	Fracture
Silicon (LAR)	2.6	4	Fracture
Silicon (HAR)	6.7	2.4	Buckling
	6.9	2.5	
	7.2	2.1	
	7.2	1.9	
	7.5	2.0	
	7.7	1.5	
	8.8	1.4	
	9.2	1.3	
	9.3	1.2	
	9.5	1.1	
	9.9	1.0	
	10.0	1.1	
	10.7	0.9	
	13.1	0.7	

Scanning electron microscopy (SEM) images obtained from the tests were used to measure the diameters of the central pillars, and the corresponding first pop-in loads were identified from the load–displacement data. The load at the first pop-in was divided by the total cross-sectional area of four central pillars, assuming that buckling initiated simultaneously in these four pillars. For example, for test 1 in Fig. 6, the average pillar diameter was measured as approximately 40 nm, and the first pop-in occurred during the first loading cycle at 5.75 μN, corresponding to a compressive stress of 1.1 GPa at the onset of buckling. For test 5, the average pillar diameter was 60 nm, and the first pop-in was observed during the second loading cycle at 27 μN, yielding a compressive stress of 2.4 GPa at the onset of buckling. Other points are calculated by following the same approach and plotted on Fig. 6.

Supplementary Information D: Failure Mode Modeling

Critical Load and Stress for Buckling

Due to the uncertainty of the indenter's position before the nanoindentation with respect to individual pillars, two extreme conditions are considered. First, the indenter axis coincides with one of the pillars. In this case, it can be assumed that the stress state is uniaxial. However, if the indenter axis is at the intersection of four nanopillars, the exerted loading is multiaxial. The distance between the indenter axis and one of the pillars is $150\sqrt{2}$ nm. Using the indenter radius, and assuming the load, P, is applied perpendicular to the indenter surface, the angle between the vertical axis and the applied load is found as 1.22°. Therefore, the vertical and horizontal components of the applied load are found as $P_y = 0.9998P$, and $P_y = 0.0212P$, respectively Therefore, the horizontal component is 2.1% of the vertical component. Moreover, buckling finite element analysis simulations on an individual pillar show that the effect on the critical buckling load of this off-axis load is 0.02% compared to uniaxial loading case, as can be seen in Figure S10. Therefore, for analytical calculations, Euler buckling model is used with uniaxial loading assumption.

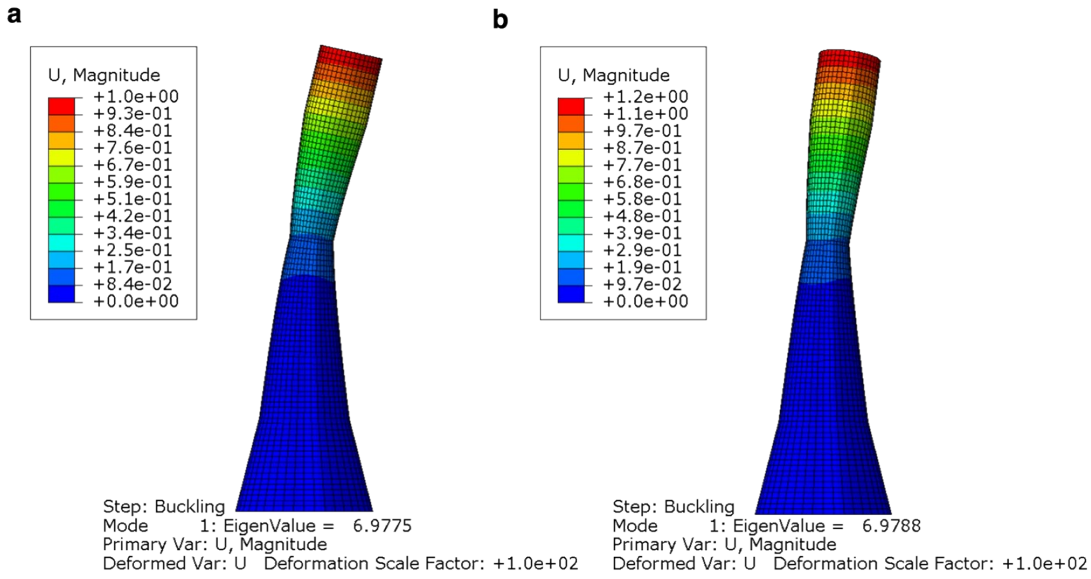

Figure S10. Finite element analysis results for (a) multiaxial and (b) uniaxial loading.

Using classical Euler buckling model, the critical load for buckling for a slender beam is calculated using equation (S7).

$$P_{cr}^{b} = \frac{\pi^2 EI}{k^2 h^2} \quad \text{(S7)}$$

Where E is the elastic modulus, I is the area moment of inertia of a pillar, h is the height, and k is the column effective length factor. Plugging in the geometrical values, and setting k to 1, the critical load for buckling is calculated using the equation (S8) for a cylindrical pillar.

$$P_{cr}^{b} = \frac{\pi^3 E d^4}{64 h^2} \quad \text{(S8)}$$

Where d is the diameter. Assuming the indenter is directly above a pillar, the critical load for buckling could be directly calculated using the dimensions and material properties. Plugging in the values, the critical buckling load for a pillar with 400 nm height and 50 nm diameter is found as 3.2 μN. Dividing both sides of equation (S8) by the cross-sectional area yields to equation (S9).

$$\sigma_{cr}^{b} = \frac{\pi^2 E d^2}{16 h^2} \quad \text{(S9)}$$

Defining aspect ratio, AR, as $AR = h/d$, critical stress for a given AR can be calculated using equation (S10).

$$\sigma_{cr}^{b} = \frac{\pi^2 E}{16 AR^2} \quad \text{(S10)}$$

Critical Load and Stress for Compressive Fracture

For the compressive fracture observed in LAR nanopillars, the critical load for fracture could be calculated using the material properties of silicon assuming the indenter is directly above a pillar.

$$P_{cr}^{f} = \frac{\pi d^2 \sigma_Y}{4} \quad \text{(S11)}$$

Where d is the diameter of the pillar and σ_Y is the yield strength. Plugging in the experimental value for yield stress of 6 GPa observed in isolated micropillars,[3–5] the critical load for fracture for a pillar with 50 nm diameter is found as 11 μN. As this value is higher than the critical load for buckling, a pillar with 50 nm diameter and 400 nm height fails due to buckling.

Dividing both sides of equation (S11) by the cross-sectional area yields to equation (S12).

$$\sigma_{cr}^{f} = \sigma_Y \tag{S12}$$

Therefore, the critical stress for material failure depends on the yield strength of the material. The critical aspect ratio, AR_c, is calculated by equating σ_{cr}^{b} and σ_{cr}^{f}, as shown in (S13).

$$\frac{\pi^2 E}{16 AR_c^2} = \sigma_Y \tag{S13}$$

Arranging the terms, the critical aspect ratio is found as given in (S14).

$$AR_c = \frac{\pi}{4}\sqrt{\frac{E}{\sigma_Y}} \tag{S14}$$

The critical aspect ratio of a silicon nanopillar is found as 4.17. For sapphire and LAR silicon, the total length of the pillars was used whereas for HAR silicon sample the length after the waist is used, which corresponds to 400 nm. At the onset of critical aspect ratio, the diameter of a pillar with 400 nm unsupported height is found as shown in (S15).

$$AR_c = \frac{400\ nm}{d} \rightarrow d = \frac{400\ nm}{AR_c} \rightarrow d = 96\ nm \tag{S15}$$

Therefore, material failure without buckling is observed in a nanopillar with a height of 400 nm and diameter of 96 nm or larger.

Supplementary Information E: Density scaling calculations

Using the SEM images of the samples, the relative density of the samples is approximated as 0.4. Then, using power low density scaling approach, the scaling exponents for each sample is calculated by solving the equation (S16), and (S17) for indentation modulus and hardness, respectively.

$$E^* = \rho_{avg}^{m*AR} \tag{S16}$$

$$H^* = \rho_{avg}^{m*AR} \tag{S17}$$

Where, $E^* = E_{sample}/E_{material}$, and, $H^* = H_{sample}/H_{material}$, ρ_{avg} is the average relative density, AR is the aspect ratio of the nanopillars, and m is the fitting exponent. The relative density of the samples is estimated using the cross-section images of the samples. The volume of an individual pillar, V_{pillar} is calculated by approximating pillars using truncated cones and cones. Then, the relative density is calculated using equation (S18).

$$\rho = V_{pillar}/V_{cell} \tag{S18}$$

Where, V_{cell} is the volume of a unit cell occupied by a single pillar.

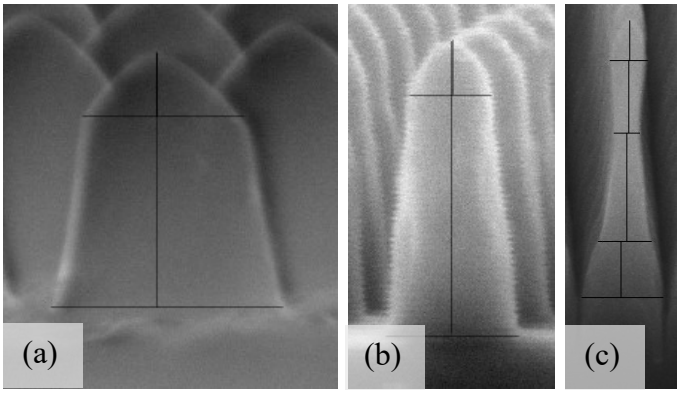

Figure S11. Measured (a) sapphire, (b) LAR and (c) HAR silicon pillars.

The relative densities for sapphire, and LAR and HAR silicon are found as 0.35, 0.28 and 0.21, respectively.

Supplementary Information F: Pencil Hardness Test on Sapphire

The samples are subjected to pencil hardness test by following the ASTM D3363 standard, with a pencil hardness tester that applies 7.5N load at a 45° angle. The sapphire sample is tested with 2H, 4B, 6H and 2B pencils as shown in Figure S12. Both LAR and HAR silicon samples are tested using a 2B pencil.

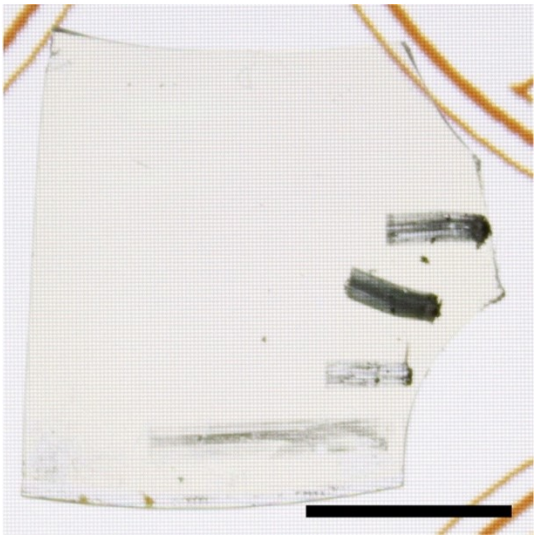

Figure S12. Pencil hardness tests on sapphire specimen. The hardness of the pencils used for testing are 2H, 4B, 6H and 2B from top to bottom Scale bar: 5 mm.

The SEM images of the tested areas are used to assess the percentage of the intact pillars. The percentage was calculated by dividing the total width of the broken segments to the width of the tested area using SEM images using ImageJ software. Another set of measurements is done using ImageJ to measure the areas. The scratched regions have a brighter color, while non-broken regions look darker in large-area SEM images, as can be seen in Figure S13. This contrast difference is used to quantify the scratched areas. Two areas are used for analysis, where gaussian blur, background subtraction and threshold commands are used to obtain the masked images. The analyzed region with 857x727 μm^2 size shows pillars in the 3.28% of the scratched area region are broken, as can be observed in the close-up SEM image in Figure S13d. These results are in line with the line width measurements.

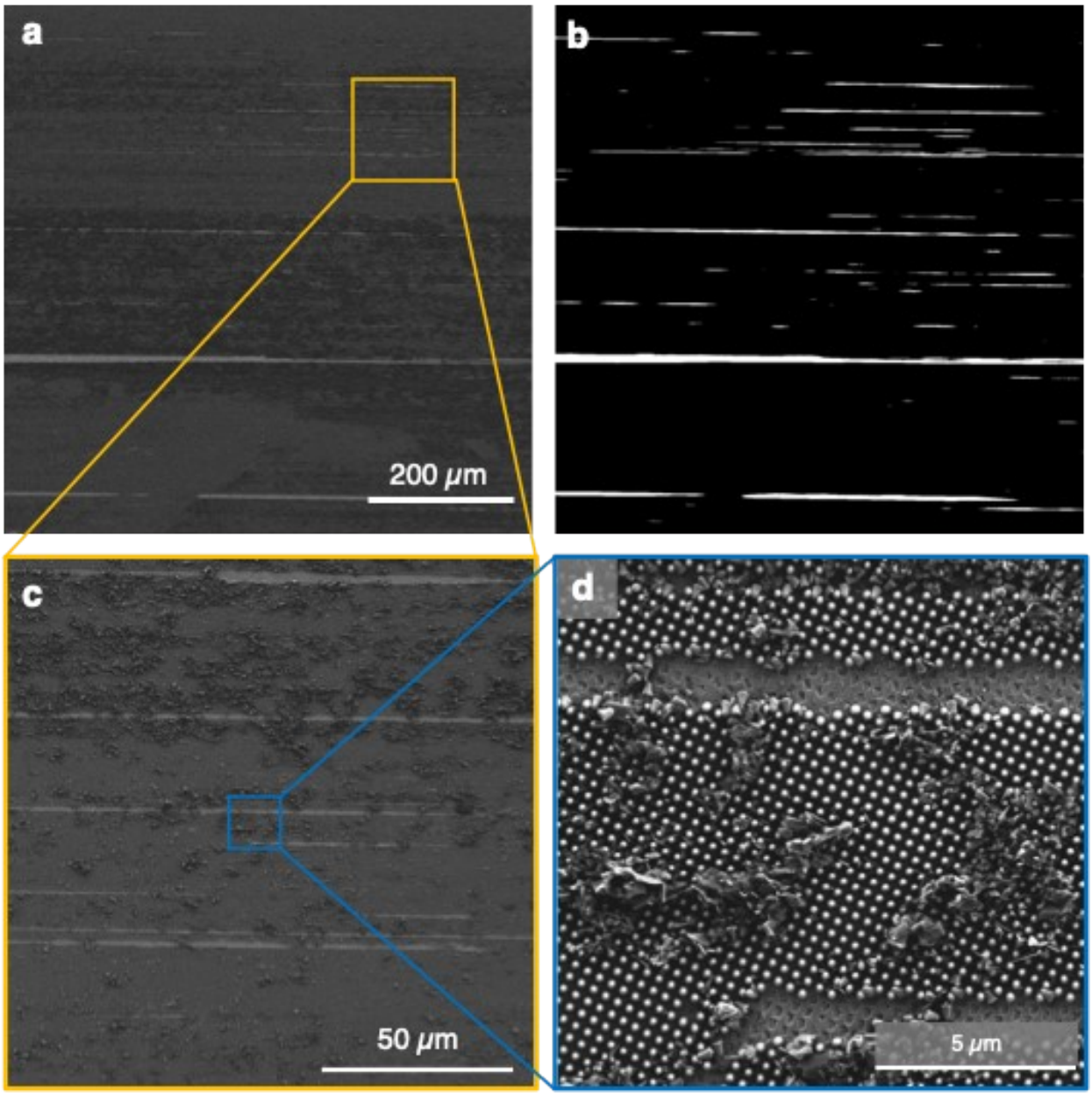

Figure S13. (a) SEM image of the scratched region with 2B pencil, and (b) masked image for scratch area calculation, (c) and (d) close-up SEM images.

The 6H pencil, which is harder than 2B, caused more pillar fracture. The corresponding SEM images for the tests with 2B and 6H pencils are shown in Figure S14.

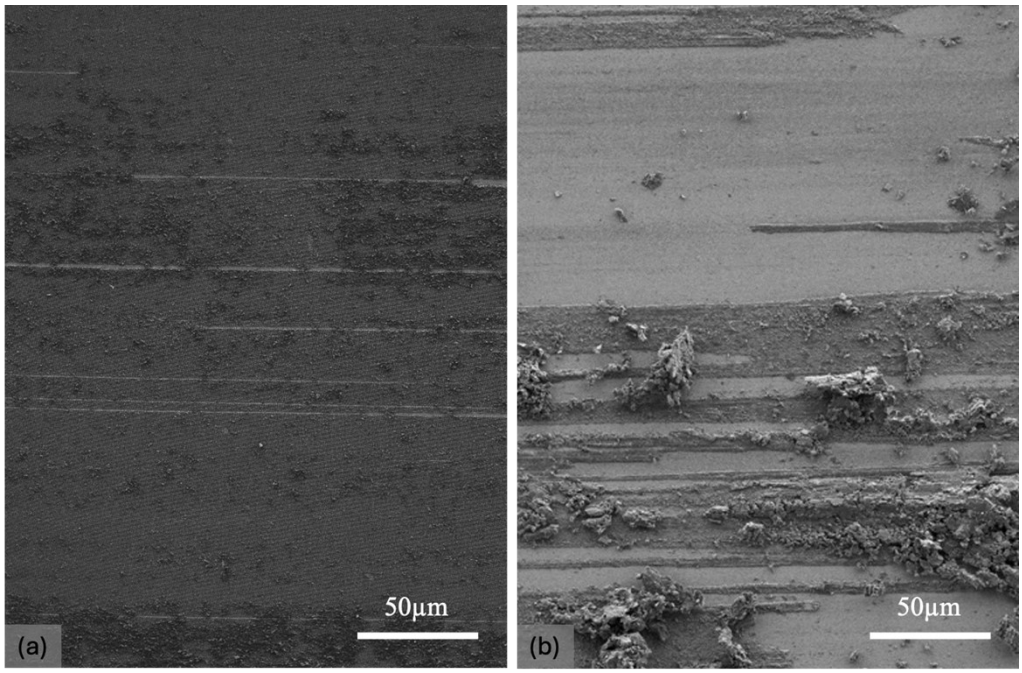

Figure S14. Large area SEM image of a region tested with (a) 2B pencil, after cleaning, and (b) 6H pencil.

References

1 K.-C. Chien and C.-H. Chang, *J. Vac. Sci. Technol., B:Nanotechnol. Microelectron.:Mater., Process., Meas., Phenom.*, 2022, **40**, 062802.

2 K.-C. Chien, N. Graff, D. Djurdjanovic and C.-H. Chang, *J. Vac. Sci. Technol., B:Nanotechnol. Microelectron.:Mater., Process., Meas., Phenom.*, 2023, **41**, 062807.

3 B. Moser, K. Wasmer, L. Barbieri and J. Michler, *J. Mater. Res.*, 2007, **22**, 1004–1011.

4 F. Östlund, K. Rzepiejewska-Malyska, K. Leifer, L. M. Hale, Y. Tang, R. Ballarini, W. W. Gerberich and J. Michler, *Adv. Funct. Mater.*, 2009, **19**, 2439–2444.

5 S. Korte, J. S. Barnard, R. J. Stearn and W. J. Clegg, *Int. J. Plast.*, 2011, **27**, 1853–1866.